Continuum Modeling of Secondary Rheology in Dense Granular Materials

David L. Henann[1,*] and Ken Kamrin[2,†]
[1]School of Engineering, Brown University, Providence, Rhode Island 02906, USA
[2]Department of Mechanical Engineering, MIT, Cambridge, Massachusetts 02139, USA
(Received 22 May 2014; published 20 October 2014)

Recent dense granular flow experiments have shown that shear deformation in one region of a granular medium fluidizes its entirety, including regions far from the sheared zone, effectively erasing the yield condition everywhere. This enables slow creep deformation to occur when an external force is applied to a probe in the nominally static regions of the material. The apparent change in rheology induced by far-away motion is termed the "secondary rheology," and a theoretical rationalization of this phenomenon is needed. Recently, a new nonlocal granular rheology was successfully used to predict steady granular flow fields, including grain-size-dependent shear-band widths in a wide variety of flow configurations. We show that the nonlocal fluidity model is also capable of capturing secondary rheology. Specifically, we explore creep of a circular intruder in a two-dimensional annular Couette cell and show that the model captures all salient features observed in experiments, including both the rate-independent nature of creep for sufficiently slow driving rates and the faster-than-linear increase in the creep speed with the force applied to the intruder.

DOI: 10.1103/PhysRevLett.113.178001 PACS numbers: 45.70.Mg, 47.57.Gc, 83.10.Ff, 83.80.Fg

Granular materials display a unique set of flow properties, which differentiate them from conventional solids or fluids. When a granular medium is subjected to boundary-driven deformation, it usually forms shear bands, the sizes of which depend upon both the geometry and the grain size [1–7]. Until recently, conventional wisdom was that outside of these shear bands the nominally quiescent material behaved as a solid. However, recent experiments of van Hecke and co-workers [8] established that this is not the case. When an intruder is placed far away from the shear band—or primary flow zone—it will move when any nonzero force is applied to it. In contrast, when there is no primary flow, a distinct yield condition is observed; i.e., a critical applied intruder force must be exceeded to move it. This vanishing of the yield stress in the presence of far-away primary flow is quite remarkable and motivates the notion of a "secondary rheology" to describe the rheological changes occurring at different locations in a granular medium due to the existence of a primary flow. These observations have been corroborated in subsequent works [9,10], establishing secondary rheology as a key open question in granular physics. For specificity, let us consider the following example from the work of Reddy, Forterre, and Pouliquen [9] which summarizes the essential phenomenology. In their work, a cylindrical rod was placed vertically in an annular Couette cell filled with grains. When the inner wall was fixed, they observed that the force applied to the rod had to exceed a critical value F_c in order to move it through the granular medium. However, when the inner wall was rotated and a primary flow consisting of an inner-wall-located shear band was formed, the yield condition vanished everywhere, enabling the rod to creep for any applied force. Importantly, several experimental observations were made about the creep phenomenology. (i) For sufficiently low inner wall speeds, secondary rheology is a rate-independent process; i.e., the rod creep speed is linearly proportional to the inner wall speed. (ii) The rod creep speed increases exponentially with the force applied to the intruder. (iii) The rod creeps faster when it is placed closer to the inner wall shear band.

As noted by Reddy, Forterre, and Pouliquen [9], these observations provide a nontrivial test for continuum models of granular flow. In fact, local approaches to continuum modeling of granular materials, such as inertial granular rheology [11–13] or soil mechanics [14,15], which relate the stress at a point to the local strain, strain rate, or locally evolved state variables, are not equipped to address secondary rheology phenomenology. Recently, we proposed a nonlocal rheology for dense granular flows, capable of quantitatively modeling primary flow fields [16–18], based on emerging concepts from the emulsions community [19,20]. The model was demonstrated to accurately describe flow fields and shear-band widths in numerous granular flow experiments in several different flow configurations [17]. Even so, it was not clear if the same model could address the distinct issue of secondary rheology, where the goal is to describe the variation of rheological properties induced by primary motion rather than the primary motion itself. In this Letter, we provide a decisive answer to this question, and to the outstanding issue of secondary rheology in general, by showing that such phenomena are all obtainable from the nonlocal model.

We begin by summarizing the nonlocal granular rheology. We denote the symmetric strain-rate tensor as $\dot{\gamma}_{ij} = (1/2)(\partial v_i/\partial x_j + \partial v_j/\partial x_i)$ with v_i the velocity vector and

x_i the spatial coordinate. We then assume that steady flow proceeds at constant volume so that $\dot{\gamma}_{kk} = 0$ [12,13,21,22] and define the equivalent shear strain rate as $\dot{\gamma} = (2\dot{\gamma}_{ij}\dot{\gamma}_{ij})^{1/2}$. Next, we introduce the symmetric Cauchy stress σ_{ij} and define the pressure $P = -(1/3)\sigma_{kk}$, the stress deviator $\sigma_{ij}' = \sigma_{ij} + P\delta_{ij}$, the equivalent shear stress $\tau = (\sigma_{ij}'\sigma_{ij}'/2)^{1/2}$, and the stress ratio $\mu = \tau/P$. Central to the model is a scalar state variable g, called the granular fluidity, which represents the susceptibility of a granular cluster to flow. Mathematically, it functions as a field variable that relates the load intensity μ to the consequent flow rate $\dot{\gamma}$, i.e., $\dot{\gamma} = g\mu$, so that the tensorial relation between the Cauchy stress and the strain rate is

$$\sigma_{ij} = -P\delta_{ij} + 2(P/g)\dot{\gamma}_{ij}, \quad (1)$$

where we have made the common assumption that the strain-rate and deviatoric Cauchy stress tensors are codirectional [12,13,21], though this is an approximation [23,24]. In a local description of granular flow, the fluidity is constitutively given as a function of the stress, in a manner consistent with Bagnold scaling [25]. Simple dimensional analysis applied to the case of homogeneous simple shearing produces a one-to-one relationship between the stress ratio μ and a dimensionless version of the strain rate called the inertial number $I = \dot{\gamma}\sqrt{d^2\rho_s/P}$, where d is the mean grain diameter and ρ_s is the grain material density. Data have verified a Bingham-like functional form for $\mu = \mu(I)$ [11], which when adopted leads to the following local description of the fluidity:

$$g_{\mathrm{loc}} = \dot{\gamma}_{\mathrm{loc}}/\mu = H(\mu - \mu_s)\sqrt{P/\rho_s d^2}[(\mu - \mu_s)/\mu b], \quad (2)$$

where μ_s is a static yield value, b is a dimensionless constant characterizing the rate-dependent response of the granular media, and H is the Heaviside step function.

While the local relation successfully describes homogeneous simple shear, in inhomogeneous flows, significant deviation from this local description is observed [16,22], which motivates a nonlocal differential relation for the granular fluidity. We have proposed the following specific functional form:

$$\nabla^2 g = (1/\xi^2)(g - g_{\mathrm{loc}}), \quad (3)$$

where $\nabla^2(\cdot)$ denotes the Laplacian operator, $\xi(\mu) = Ad/\sqrt{|\mu - \mu_s|}$ is the stress-dependent cooperativity length, and A is a dimensionless material parameter called the nonlocal amplitude. In the absence of the $\nabla^2 g$ term, the model reduces to the local description with $g = g_{\mathrm{loc}}$; however, when flow inhomogeneity is present, this term accounts for nonlocal effects and quantitatively captures the loss of local constitutive uniqueness between μ and I.

Next, we apply our nonlocal model to the problem of secondary rheology, by using finite-element calculations in the commercial package ABAQUS/STANDARD [26]. For computational efficiency, we consider a two-dimensional analogue of the experiments of Reddy, Forterre, and Pouliquen [9], pictured in Fig. 1. The geometry is a planar annular shear cell with rough walls at an inner radius R_i and outer radius R_o. The inner wall is specified to rotate at a fixed rate Ω, and the outer wall does not rotate but may move radially so as to impart a confining pressure P_a. A circular intruder with diameter D, which we specify to be rigid and frictionless, is located at a distance L away from the inner wall. Following Ref. [9], we take $R_i/d = 60$, $R_o/d = 180$, and $D/d = 2$, throughout, and consider different values of L/d. The value of outer radius is sufficiently large so as not to affect the calculation results, consistent with experiments. Finally, in our calculations, either the speed of the intruder V or the force applied to the intruder F is specified. We then calculate the steady flow fields predicted by the nonlocal rheology using ABAQUS. The governing partial differential equations are the equilibrium equations $\partial\sigma_{ij}/\partial x_j = 0_i$, where inertia is neglected, since we are considering a quasistatic process and there is no gravitational body force since we are in two dimensions, and the differential relation for the granular fluidity (3). These are solved in conjunction with the constitutive equations (1) and (2) by means of a user element subroutine in ABAQUS. The mechanical boundary conditions are as described above, and, for the fluidity boundary conditions, we specify that $n_i(\partial g/\partial x_i) = 0$ at the inner and outer walls, where n_i is the outward surface normal. A detailed discussion of the intruder boundary conditions is given in Supplemental Material [27]. The necessary material parameters are $\{\mu_s, b, A\}$. Following previous work involving glass beads [13,17,28], we take $\mu_s = 0.3819$ and $b = 0.9377$. For the two-dimensional problem, we take $A = 1.8$ (see Supplemental Material [27] for a justification of this selection).

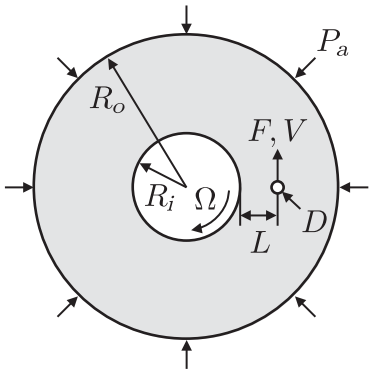

FIG. 1. Schematic of the two-dimensional analogue of the experiments of Ref. [9].

In our first set of simulations, we determine the critical force F_c. To this end, we fix the inner wall ($\Omega = 0$) and specify normalized intruder velocities $V\sqrt{\rho_s/P_a}$ spanning from 10^{-7} to 10^{-2}. Each calculation quickly reaches a

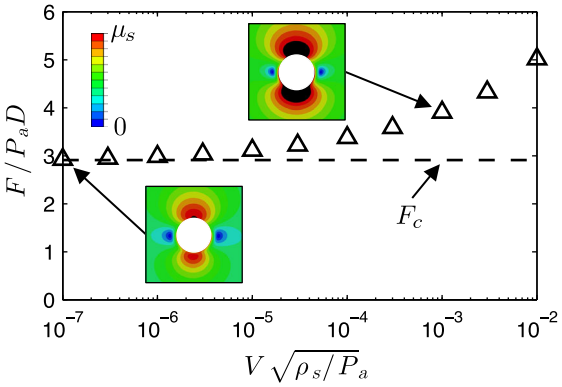

FIG. 2 (color online). Force applied to the intruder as a function of intruder velocity when the inner wall is fixed $\Omega = 0$. The dashed line indicates the rate-independent critical force $F_c/P_aD = 2.91$. Insets show contour plots of the stress ratio μ in the region of the intruder; black regions denote where $\mu > \mu_s$.

steady state, and we plot the normalized steady-state applied force F/P_aD as a function of velocity in Fig. 2 (see Supplemental Material [27] for a demonstration of mesh insensitivity). This result was observed to be identical for $L/d = 18$, 24, and 34. For normalized velocities greater than approximately 10^{-5}, we see a clear rate dependence. In the calculations, this corresponds to a non-negligible portion of the domain achieving $\mu > \mu_s$ so that the g_{loc} term in (3) has a substantial effect in this region. See the contour plot inset of the stress ratio μ in the region of the intruder in Fig. 2 corresponding to $V\sqrt{\rho_s/P_a} = 1 \times 10^{-3}$. The white region represents the intruder, which is moving upwards, and the region in which $\mu > \mu_s$ is denoted as black. Much of the region in front of and behind the intruder has met this condition. However, for $V\sqrt{\rho_s/P_a}$ less than 10^{-5}, the force becomes nominally rate independent, plateauing to a constant value of $F_c/P_aD = 2.91$, which we denote as the critical force. In this case, the region around the intruder where $\mu > \mu_s$ is significantly smaller (see the inset in Fig. 2 for $V\sqrt{\rho_s/P_a} = 1 \times 10^{-7}$). The relation of Fig. 2 is consistent with analogous experimental observations [see Fig. 1(c) of Ref. [9] and Fig. 2(b) of Ref. [10]].

Next, we examine creep phenomenology when the inner wall is rotated. In our calculations, we first apply a force to the intruder less than F_c and hold the force constant for a period of time. During this time, the intruder does not creep, and the granular fluidity is zero everywhere. The inner wall is then moved at a fixed speed in a tangential direction which opposes the force applied to the intruder (see Fig. 1). This sets up a primary flow characterized by an inner-wall-located shear band and induces a granular fluidity field which is nonzero everywhere. This fluidity field decays with radial distance from the inner wall and is quite small in the region of the intruder. However, fluidization of this region causes the intruder to begin creeping.

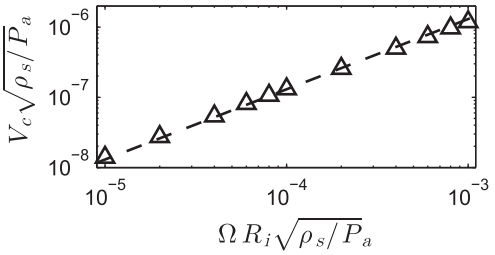

FIG. 3. Intruder creep speed as a function of inner wall speed for $F/F_c = 0.75$ and $L/d = 24$, demonstrating nominal rate independence in a range of sufficiently small inner wall speeds; the dashed line denotes the linear relation $V_c/\Omega R_i = 1.3 \times 10^{-3}$.

Steady state is quickly reached, and we denote the constant creep speed of the intruder as V_c. Figure 3 shows the normalized intruder creep speed $V_c\sqrt{\rho_s/P_a}$ as a function of the normalized inner wall speed $\Omega R_i\sqrt{\rho_s/P_a}$ for a fixed applied force $F/F_c = 0.75$ and intruder position $L/d = 24$, indicating a linear relationship with $V_c/\Omega R_i = 1.3 \times 10^{-3}$. This is a hallmark of rate independence and demonstrates that the material time scale $d\sqrt{\rho_s/P_a}$ is nominally irrelevant for $\Omega R_i\sqrt{\rho_s/P_a} \lesssim 10^{-3}$ and that the time scale dictating the creep speed of the intruder is that imposed by the inner wall speed. As the inner wall speed is increased further, a deviation from linearity is observed in the calculations, indicating an increased role of the local rheology. This rate-independent regime of creep was observed in all configurations of experiments [see Fig. 4(a) of Ref. [8], Fig. 2(b) of Ref. [9], and Fig. 3 of Ref. [10]].

The creep speed in the rate-independent regime depends on the force applied to the intruder F/F_c as well as the distance between the intruder and the inner wall L/d. (We did not examine the effect of intruder size D/d in this study.) The calculated dependence is shown as symbols in Fig. 4 for $L/d = 18$, 24, and 34 and $\Omega R_i\sqrt{\rho_s/P_a} = 1 \times 10^{-5}$. For $F < F_c$, we observe that (i) the intruder

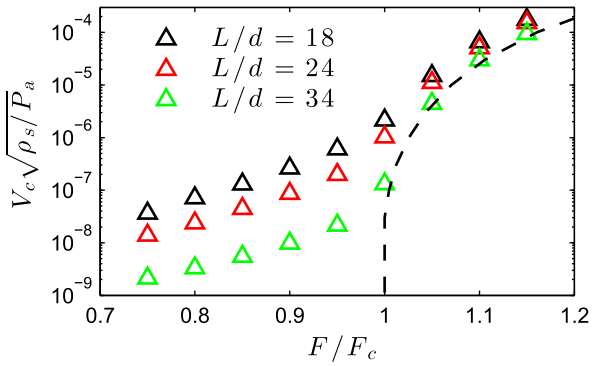

FIG. 4 (color online). Intruder creep speed as a function of applied force for $L/d = 18$, 24, and 34 and $\Omega R_i\sqrt{\rho_s/P_a} = 1 \times 10^{-5}$. Simulated creep data are shown as symbols; the dashed line represents the drag force versus intruder velocity relation of Fig. 2.

creeps faster for higher applied force and (ii) the intruder creeps faster when it is closer to the inner wall for all applied forces—both intuitive notions. What is nonintuitive is that the relation between the creep speed and applied force for $F < F_c$ and fixed L/d is nonlinear. In fact, the relation in this range is exponential in character, consistent with experiments (see Fig. 4 of Ref. [9] and Fig. 4 of Ref. [10]). Also plotted in Fig. 4 as a dashed line is the drag force versus intruder velocity relationship of Fig. 2. As the applied force is increased past F_c, the simulated data for different L/d converge and asymptotically approach the rate-dependent part of this relation, which is dominated by the local rheology rather than nonlocal effects. The convergence of the data around $F = F_c$ is qualitatively consistent with experiments [9]. (For more discussion of this point and additional simulated creep data, see Supplemental Material [27].)

The faster-than-linear character of the results of Fig. 4 may be understood by using the following examination of the differential relation (3), while the specifically exponential shape observed is assessed in Supplemental Material [27]. The differential relation (3) has the structure of an inhomogeneous Helmholtz equation with g_{loc} playing the role of a "source" term. When subjected to the boundary condition $n_i(\partial g/\partial x_i) = 0$ at the walls, the fluidity field will be zero everywhere if $g_{\mathrm{loc}} = 0$ (or $\mu < \mu_s$) everywhere and will be nonzero everywhere if $g_{\mathrm{loc}} > 0$ (or $\mu > \mu_s$) *anywhere*. In the present simulations, rotation of the inner wall sets up a small region at the inner wall where $g_{\mathrm{loc}} > 0$—a shear band—and, as one moves away from the shear band, the fluidity undergoes an exponential-like decay but remains nonzero. This fluidity field may equivalently be thought of as a radially dependent viscosity field with the viscosity lower closer to the shear band. This justifies the increase of creep speed with decreasing L/d. A simplistic Stokes-flow view of the creep problem would indicate that the creep speed and applied force should be linearly related. The fact that this is not observed indicates that the presence of the intruder has an important influence on the fluidity field. This effect is summarized in Fig. 5. Figure 5(a) shows contour plots of the stress ratio field μ in the region of the intruder (which is white and moving upwards) for two values of the applied force F/F_c, 0.75 and 0.95, $L/d = 24$, and $\Omega R_i\sqrt{\rho_s/P_a} = 1 \times 10^{-5}$. In both cases, the stress ratio μ reaches and just exceeds the critical value μ_s, leading to $g_{\mathrm{loc}} > 0$ in a very small region of the intruder boundary. In a sense, this "activates" an additional source at the intruder. As can be seen in Fig. 5(a), while this region is indiscernible for $F/F_c = 0.75$, more of the region surrounding the intruder reaches μ_s for the case of $F/F_c = 0.95$, and, as a consequence, the "source" is stronger and the fluidity is increased in the region of the intruder. Figure 5(b) shows the fluidity g along a radial path from the inner wall to the intruder for $F/F_c = 0.75$ and 0.95. Near the inner wall, away from the intruder, the fluidity field is essentially the same in both cases. However, in the region of the intruder, the stronger source in the higher force case leads to a local fluidity which is approximately 6 times greater—or, equivalently, a viscosity which is 6 times less. This decrease in viscosity combined with the greater applied force leads to the faster-than-linear increase in creep speed with force observed in Fig. 4.

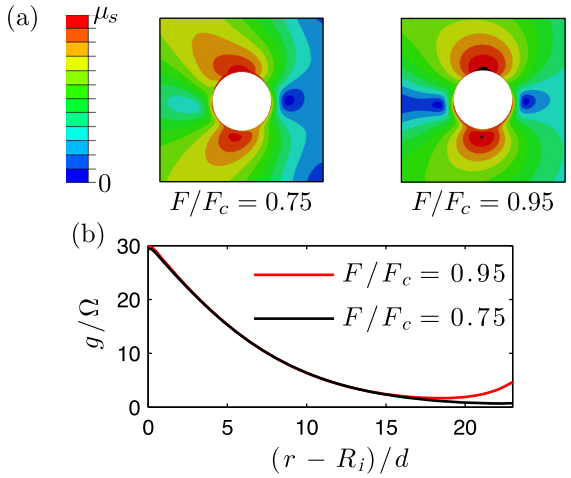

FIG. 5 (color online). (a) Contour plots of the stress ratio μ in the region of the intruder during steady creep for $F/F_c = 0.75$ and 0.95, $L/d = 24$, and $\Omega R_i\sqrt{\rho_s/P_a} = 1 \times 10^{-5}$. (b) The granular fluidity along a radial path between the inner wall and the intruder for these two cases.

In conclusion, we have demonstrated that the nonlocal granular rheology is capable of describing the phenomenology of secondary rheology [8–10], offering a means for more thorough, quantitative interpretation of secondary rheology experiments and providing a complete description of all relevant fields, including those that might be difficult to measure experimentally, such as stress. Finally, the fact that the model describes both primary flow fields [17] as well as secondary rheology demonstrates the generality of the model and paves the way for modeling other complex phenomena in dense granular flow, such as flow anisotropy [10] and nonmonotonic rheology [29,30].

D. L. H. acknowledges funds from the Brown University School of Engineering, and K. K. acknowledges funds from NSF-CBET-1253228 and the MIT Department of Mechanical Engineering.

*david_henann@brown.edu
†kkamrin@mit.edu

[1] G. D. R. MiDi, Eur. Phys. J. E **14**, 341 (2004).
[2] D. E. Mueth, G. F. Debregeas, G. S. Karczmar, P. J. Eng, S. R. Nagel, and H. M. Jaeger, Nature (London) **406**, 385 (2000).
[3] D. Fenistein and M. van Hecke, Nature (London) **425**, 256 (2003).

[4] D. Fenistein, J. W. van de Meent, and M. van Hecke, Phys. Rev. Lett. **92**, 094301 (2004).
[5] D. Fenistein, J. W. van de Meent, and M. van Hecke, Phys. Rev. Lett. **96**, 118001 (2006).
[6] X. Cheng, J. B. Lechman, A. Fernandez-Barbero, G. S. Grest, H. M. Jaeger, G. S. Karczmar, M. E. Möbius, and S. R. Nagel, Phys. Rev. Lett. **96**, 038001 (2006).
[7] S. Siavoshi, A. V. Orpe, and A. Kudrolli, Phys. Rev. E **73**, 010301(R) (2006).
[8] K. Nichol, A. Zanin, R. Bastien, E. Wandersman, and M. van Hecke, Phys. Rev. Lett. **104**, 078302 (2010).
[9] K. A. Reddy, Y. Forterre, and O. Pouliquen, Phys. Rev. Lett. **106**, 108301 (2011).
[10] E. Wandersman and M. van Hecke, Europhys. Lett. **105**, 24002 (2014).
[11] F. da Cruz, S. Emam, M. Prochnow, J.-N. Roux, and F. Chevoir, Phys. Rev. E **72**, 021309 (2005).
[12] P. Jop, Y. Forterre, and O. Pouliquen, Nature (London) **441**, 727 (2006).
[13] K. Kamrin, Int. J. Plast. **26**, 167 (2010).
[14] A. Schofield and P. Wroth, *Critical State Soil Mechanics* (McGraw-Hill, New York, 1968).
[15] R. M. Nedderman, *Statics and Kinematics of Granular Materials* (Cambridge University Press, Cambridge, England, 1992).
[16] K. Kamrin and G. Koval, Phys. Rev. Lett. **108**, 178301 (2012).
[17] D. L. Henann and K. Kamrin, Proc. Natl. Acad. Sci. U.S.A. **110**, 6730 (2013).
[18] D. L. Henann and K. Kamrin, Int. J. Plast. **60**, 145 (2014).
[19] J. Goyon, A. Colin, G. Ovarlez, A. Ajdari, and L. Bocquet, Nature (London) **454**, 84 (2008).
[20] L. Bocquet, A. Colin, and A. Ajdari, Phys. Rev. Lett. **103**, 036001 (2009).
[21] C. H. Rycroft, K. Kamrin, and M. Z. Bazant, J. Mech. Phys. Solids **57**, 828 (2009).
[22] G. Koval, J.-N. Roux, A. Corfdir, and F. Chevoir, Phys. Rev. E **79**, 021306 (2009).
[23] S. Luding, Part. Sci. Technol. **26**, 33 (2007).
[24] M. Depken, J. B. Lechman, M. van Hecke, W. van Saarloos, and G. S. Grest, Europhys. Lett. **78**, 58001 (2007).
[25] R. A. Bagnold, Proc. R. Soc. A **225**, 49 (1954).
[26] ABAQUS, reference manuals, 2013.
[27] See Supplemental Material at http://link.aps.org/supplemental/10.1103/PhysRevLett.113.178001 for a detailed discussion of the intruder boundary conditions, a justification of our choice of A, a mesh sensitivity study, additional simulated creep data, and explanations for exponential creep-rate behavior.
[28] P. Jop, Y. Forterre, and O. Pouliquen, J. Fluid Mech. **541**, 167 (2005).
[29] J. A. Dijksman, G. H. Wortel, L. T. H. van Dellen, O. Dauchot, and M. van Hecke, Phys. Rev. Lett. **107**, 108303 (2011).
[30] O. Kuwano, R. Ando, and T. Hatano, Geophys. Res. Lett. **40**, 1295 (2013).